

Instability of isolated compressible entropy-stratified vortices

Igor Men'shov^{a)} and Yoshiaki Nakamura

Department of Aerospace Engineering, Nagoya University, Furo-cho, Chikusa-ku, Nagoya 464-8603, Japan

(Received 11 November 2004; accepted 19 November 2004; published online 28 January 2005)

The normal mode linear analysis is applied to investigate the stability of a circular isolated compressible vortex with the emphasis on studying the effect of entropy stratification of the basic flow on stability properties. We study a family of vortices that have zero total circulation, with the swirl velocity being presented by a Taylor-type distribution in the radial direction. The stratification of entropy is modeled by a Gaussian two-parametric profile whose parameters control the maximal deviation from the homentropic distribution and the extent of the entropic zone. Results presented concern the effect of these parameters and the vortex intensity on instability characteristics. In particular, in the case of homentropic flow, vortices considered are found to be stable only for sufficiently high intensities and cease to be stable as the intensity weakens. As an example of the situation where unstable normal modes can be excited, the scattering of sound waves by the vortex flow is considered. By simulating this process numerically, we show that the scattered field becomes unstable in the course of time and acquires a typical periodical pattern in polar angle. The characteristics of this instability (viz., the growth rate and the azimuthal phase frequency) coincide with those of the linear analysis very closely. This fact shows conclusively that the instability is caused by the induction of unstable normal modes in the vortex by means of sound irradiation.

© 2005 American Institute of Physics. [DOI: 10.1063/1.1851451]

I. INTRODUCTION

Locally columnar vortices in which the vorticity has large magnitude in the neighborhood of the center line are common in aerodynamics and geophysical flow dynamics. Such vortices are presented, for example, in the wake flow behind a blunt body. The shear layer on the body surface is not a stable form; it tends to roll up, the vorticity being concentrated more and more in the rolled-up zones until it presented the occurrence of concentrated vortices. In geophysical flows, columnar vortices such as tornadoes appear due to the planetary rotation. It tends to make the flow two dimensional (in accordance of the Taylor–Proudman theorem), and therefore a local vorticity acquires a strong vertical coherence evolving toward columnar vortical structures similar to Taylor columns.

Moreover, vortex columns, so-called vortex tubes (or “worms”), are encountered in three-dimensional turbulent flows. This fact was detected in experimental observations of Douady *et al.*¹ and Jiménez *et al.*² that revealed the existence of coherent and ordered tubelike structures in isotropic turbulent flows. The vortex tubes undergo instabilities followed by vortex breakdown which is believed to be a strong mechanism of the energy transfer from larger scales to smaller scales in the turbulence decay.³ Flow parameters in these vortex tubes are not well understood, yet model experiments of Bottausci and Petitjeans⁴ have shown a radially decreasing circulation outside the core that may point to the structure of an isolated vortex.

The present paper addresses the stability of an isolated

vortex which belongs to the class of vortices introduced by Carton and McWilliams.⁵ The vortex is said to be isolated when its vorticity core is surrounded by an annulus of opposite vorticity. Inversely from usual monotonic vortices with one-signed vorticity, which have a finite circulation at infinity, an isolated vortex has the circulation vanished at a finite distance from the core and is characterized by a strong azimuthal shear flow in the peripheral region.

There are lots of investigations that have been carried out to the present day, which are devoted to the stability of vortical and swirling flows (see Ref. 6 and references therein). However, most of these studies concern the model of incompressible fluid. Compressible vortices, meanwhile, are a significant feature of many fluid flows of theoretical and practical interest: Vortices produced by the diffraction of shock waves over obstacles,⁷ strong leadingedge and tip vortices generated by wings,⁸ and accretion disks in binary star systems are just a few examples. More comprehensive discussion of compressible vortices can be found in a survey by Bershader.⁹

Despite the frequent occurrence of compressible vortices in the literature, relatively little is known about their stability properties; the rather extensive vortex stability literature contains only a minuscule percentage of publications regarding the compressibility effect. Howard¹⁰ investigated the stability of an arbitrary axisymmetric swirling flow to axisymmetric disturbances by means of integral techniques and derived the sufficient conditions for this stability to exist. Broadbent and Moore¹¹ investigated the stability of an unbounded homentropic Rankine vortex and found the existence of nonaxisymmetric unstable modes. Chan *et al.*¹² studied compressible vortices of a more general structure and showed that vortices with one-signed smoother (but also finite) vorticity distribu-

^{a)}Author to whom correspondence should be addressed. Electronic mail: menshov@nuae.nagoya-u.ac.jp

tions than the Rankine vortex are also unconditionally unstable (the instability is not peculiar to a discontinuity in the vorticity distribution). They also considered the vortex with an infinite Gaussian-type vorticity profile and found it, on the other hand, to be neutrally stable for all reference Mach numbers.

For isolated vortices with zero circulation at infinity, stability analyses have been fulfilled for the most part also on the assumption that flow is incompressible. Carton and McWilliams⁵ studied the evolution of two-dimensional perturbations in an axisymmetric vortex and found the instability that results in the formation of multipolar vortex structures like tripoles and quadrupoles. Similar results were obtained by Orlandi and Carnevale¹³ for isolated vortices in a rotating fluid of finite depth. It was shown that the azimuthal shear is the major mechanism of the multipolar formation and also that the order of the multipole depends on the steepness of the velocity distribution in the opposite vorticity region surrounding the vortex core (see Refs. 14 and 15). Gallaire and Chomaz¹⁶ studied the three-dimensional instability of the family of isolated vortices introduced by Carton and McWilliams⁵ by the direct numerical simulation of the linear impulse response. The results of this study showed that whereas the axisymmetric mode is the most unstable mode (the centrifugal instability), yet larger azimuthal modes are also destabilized as the steepness of the opposite vorticity annulus zone is increased.

The focus of the present paper is to investigate the effect of compressibility and the effect of entropy stratification of the basic flow on stability properties of isolated vortices. The flow to be examined represents a planar circular inviscid compressible vortex. The swirl velocity has a Gaussian distribution in the radial direction (for the incompressible fluid model, the Gaussian vortex was studied by Gent and McWilliams¹⁷). To model the distribution of entropy, a two-parametric Gaussian profile is used whose parameters control the maximal deviation from the homentropic distribution and the extent of the entropy core. The linear-stability analysis is performed to find unstable normal modes and study the effect of flow parameters, such as vortex intensity and two entropy-controlling parameters, on instability characteristics.

Another purpose of the present paper is to demonstrate how unstable normal modes predicted by the linear-stability analysis can be realized in a real situation. To this end, we consider a well-studied problem on the scattering of plane monochromatic sound waves by a vortex flow. By numerically simulating the scattering process, we show that after a period of stable prelude unstable normal modes are in fact induced in the scattered field and characteristics of these modes, such as the growth rate and the azimuthal phase velocity, well agree with those obtained with the normal mode linear-stability analysis.

The paper is organized as follows. In Sec. II the linear-stability analysis is presented for a Gaussian vortex flow with a nonuniform distribution in entropy. The eigenvalue problem for the complex eigenfrequency is formulated and its solution is discussed. Low order unstable modes are first analyzed for two typical situations that are referred to as overentropic and underentropic vortex. Hereafter the vortex

is termed overentropic when entropy increases in the core and underentropic otherwise, i.e., when entropy lowers in the core. Then the effect of the entropy zone extent on flow stability is investigated. Lastly, the stability of higher-order modes is discussed. In Sec. III the scattering of plane monochromatic sound waves by the vortex flow is numerically simulated with the linearized Euler equations (LEE) model to obtain excitation of unstable modes in the scattered field. The description of the numerical method for solving the scattering problem is presented. The numerical method is validated by analyzing the computed scattered field for the period of stable scattering and comparing its characteristics with those predicted by theory and other (DNS) simulations. After the instability appears, the time behavior of the scattered field is examined with the fast Fourier transform (FFT) analysis, and the obtained growth rate and azimuthal phase frequency are compared with those of the normal mode linear-stability analysis. Conclusions are made in Sec. IV.

II. LINEAR-STABILITY ANALYSIS

A. Formulation

We consider the two-dimensional equations governing the motion of a nondissipative compressible fluid. By using polar coordinates (r, ϕ) , these equations may be written in the following nondimensional form:

$$\frac{\partial \rho}{\partial t} + \frac{1}{r} \frac{\partial r \rho u}{\partial r} + \frac{1}{r} \frac{\partial r \rho v}{\partial \phi} = 0, \quad (1)$$

$$\frac{\partial u}{\partial t} + u \frac{\partial u}{\partial r} + v \frac{\partial u}{\partial \phi} - \frac{v^2}{r} + \frac{1}{\rho} \frac{\partial p}{\partial r} = 0, \quad (2)$$

$$\frac{\partial v}{\partial t} + u \frac{\partial v}{\partial r} + v \frac{\partial v}{\partial \phi} + \frac{uv}{r} + \frac{1}{r \rho} \frac{\partial p}{\partial \phi} = 0, \quad (3)$$

$$\frac{\partial s}{\partial t} + u \frac{\partial s}{\partial r} + v \frac{\partial s}{\partial \phi} = 0. \quad (4)$$

Here u , v , ρ , and p denote nondimensional radial and azimuthal components of the velocity vector, density, and pressure, respectively, and s is the exponential of nondimensional entropy, which is written in terms of nondimensional density and pressure as $s = p/\rho^\gamma$, where γ is the ratio of the specific heats at constant pressure and volume. The equations were made nondimensional by using r_0 , $r_0 \sqrt{\rho_\infty / \sqrt{p_\infty}}$, $\sqrt{p_\infty / \rho_\infty}$, p_∞ , and ρ_∞ as scales for length, time, velocity, pressure, and density, respectively, where r_0 is the vortex core radius and the subscript of infinity denotes nondisturbed parameters far from the core.

Equations (1)–(4) admit a class of stationary vortex-type solutions, which do not depend on the polar angle ϕ and have zero radial velocity. These solutions are defined by the following two relations:

$$\frac{dp}{dr} = \frac{\rho v^2}{r}, \quad s = p/\rho^\gamma, \quad (5)$$

which can be integrated providing that distributions in the radial direction of two parameters are given, e.g., $v=V(r)$ and $s=S(r)$.

The linear-stability analysis is performed by considering the behavior of an infinitesimal disturbance superposed on the stationary vortex that is defined by the solution of Eq. (5). Thus, the disturbed field is given by

$$\rho + R, \quad u, \quad v + V, \quad p + P, \quad \text{and} \quad s + S, \quad (6)$$

where capitals denote flow parameters of the stationary vortex. The disturbance is analyzed into normal modes, when all flow parameters have the similar (t, ϕ) dependence given by $\exp[i(\lambda t + m\phi)]$, e.g.,

$$p(t, r, \phi) = p(r) \exp[i(\lambda t + m\phi)], \quad (7)$$

with λ and m being a constant, generally complex, and a positive integer, respectively. The disturbance amplitudes $p(r)$, $u(r)$, $v(r)$, $\rho(r)$, and $s(r)$ are defined by the linear system, which results from linearizing Eqs. (1)–(4):

$$i r \sigma \rho + \frac{d(r R u)}{dr} + i m R v = 0, \quad (8)$$

$$i r \sigma R u - 2 R V v - V^2 \rho + r \frac{dp}{dr} = 0, \quad (9)$$

$$i r \sigma R v + R \left(V + r \frac{dV}{dr} \right) u + i m p = 0, \quad (10)$$

$$i \sigma s + \frac{dS}{dr} u = 0, \quad (11)$$

$$s - \frac{S}{P} (p - C^2 \rho) = 0, \quad (12)$$

where $\sigma = \lambda + mV/r$ is the Doppler-shifted frequency, and $C = \sqrt{\gamma P/R}$ is the speed of sound in the basic stationary flow.

These equations can then be recast in new variables ξ and η that are related to the velocity amplitudes u and v as

$$u = \frac{i \sigma \xi}{R}, \quad v = \frac{1}{R} \left[i \sigma \eta - r \frac{d(V/r)}{dr} \xi \right]. \quad (13)$$

So defined, the vector (ξ, η) resembles a compressible analog of the Lagrangian displacement introduced by Chandrasekhar¹⁸ for incompressible swirling flows.

Eliminating η , ρ , and s between the resulting equations, finally we obtain the system of two differential equations for ξ and p :

$$\frac{dp}{dr} = \left(\frac{r \Omega^2}{C^2} - \frac{2m}{r \sigma} \Omega \right) p + \left[\sigma^2 - \frac{2\Omega}{r} \frac{d(r^2 \Omega)}{dr} + r \Omega^2 E \right] \xi, \quad (14)$$

$$\frac{1}{r} \frac{d(r \xi)}{dr} = \left(\frac{m^2}{r^2 \sigma^2} - \frac{1}{C^2} \right) p + \left(\frac{2m}{r \sigma} \Omega - E \right) \xi, \quad (15)$$

where $\Omega = V/r$ is the angular velocity of the basic flow and

$$E = \frac{1}{\gamma} \frac{d \ln S}{dr}. \quad (16)$$

Equations (14) and (15) are solved for all domain $0 \leq r \leq +\infty$ under the boundary condition

$$\xi = 0 \quad \text{when} \quad r = 0. \quad (17)$$

Another condition is that the solution must be uniformly bounded, i.e.,

$$|\xi|, |p| \leq M < +\infty \quad \text{for} \quad 0 \leq r \leq +\infty, \quad (18)$$

where M is a positive finite constant. Taking an integer for m , Eqs. (14)–(18) describe an eigenvalue problem on λ , which is generally complex. Its real part, $\lambda_r = \text{Re}(\lambda)$, represents the azimuthal phase frequency, while the imaginary part, $\lambda_i = \text{Im}(\lambda)$, defines the temporal growth (or damping) rate of disturbances. The phase velocity is given by λ_r/m .

It should be noted that neither the equations nor the boundary conditions involve the complex unit i . Consequently, the complex conjugate of the problem shows that if ξ and p are eigenfunctions related to an eigenvalue λ for some m then ξ^* , p^* , and λ^* are also eigenfunctions and eigenvalue for the same m . In other words, the spectrum of eigenvalues must be symmetric about the real axis. To each decaying mode there must be a corresponding growing mode. Hence, existing of a complex eigenvalue ensures instability of the basic vortex flow.

B. The basic vortex flow

The flow of a circular inviscid vortex is completely defined by distributions of any two flow parameters in radial direction. Assuming $V(r)$ and $S(r)$ for the swirl velocity and the entropy function (the exponential of entropy), respectively, the distributions of other parameters, such as pressure, density, and sound velocity are determined from Eq. (5) and can be written as

$$P = Z^{\gamma/\gamma-1}, \quad R = Z^{1/\gamma-1} S^{-1/\gamma}, \quad C = \sqrt{\gamma Z S^{1/\gamma}}, \quad (19)$$

where $Z(r)$ is given by

$$Z(r) = 1 - \frac{\gamma-1}{\gamma} \int_r^{+\infty} y S(y)^{-1/\gamma} [\Omega(y)]^2 dy. \quad (20)$$

We use the family of Gaussian vortices, in which the swirl velocity is defined as

$$V(r) = \mu r \exp[0.5(1 - r^2)]. \quad (21)$$

Here μ is the maximal nondimensional swirl velocity, which can also be recognized as the maximal Mach number (based on the sound velocity at infinity) multiplied by the factor $\sqrt{\gamma}$. The stability of these vortices in incompressible fluid was first studied by Gent and McWilliams¹⁷ and more recently by Smyth and McWilliams.¹⁹ Flor and van Heijst²⁰ have shown that the Gaussian distribution fits their experimental vortices.

For modeling the entropy distribution, we use the following two-parameter profile:

$$S(r) = [1 + \theta \exp(-\alpha r^2)]^{-\gamma}, \quad (22)$$

where θ is a constant ($\theta > -1$) that characterizes the maximal deviation from the homentropic distribution and α is a constant ($\alpha > 0$) that models the spread of the entropy-stratified region. Similar entropy profiles were used by Chan *et al.*¹²

For the foregoing profiles $V(r)$ and $S(r)$, the function $Z(r)$ of Eq. (20) becomes

$$Z(r) = 1 - \frac{\gamma-1}{2\gamma} \mu^2 \left[1 + \frac{\theta}{1+\alpha} \exp(-\alpha r^2) \right] \exp(1-r^2). \quad (23)$$

For the pressure at the origin to be positive, it must be $Z(0) \geq 0$. The latter imposes the following restriction on the modeling parameters:

$$\mu^2 \leq \frac{2\gamma(1+\alpha)}{(\gamma-1)(1+\alpha+\theta)}. \quad (24)$$

As the velocity in the vortex increases, the pressure lowers until it reaches zero at the center. Further increase in velocity beyond the limit (24) leads to the regime when gas evacuates a region in the vicinity of the center. This regime is beyond the scope of the present study and is not considered here.

C. Solving the eigenvalue problem

The eigenvalue problem given by Eqs. (14) and (15) and boundary conditions (17) and (18) is solved numerically. To do this, first analytical asymptotic solutions are obtained near the origin, when $r \rightarrow 0$, and for the far field, when $r \rightarrow +\infty$.

As $r \rightarrow 0$, the angular velocity Ω approaches a value $\Omega_0 = \mu$, and the solution is governed by the following asymptotic equations:

$$\frac{dp}{dr} = -\frac{2m}{\sigma_0 r} \Omega_0 p + (\sigma_0^2 - 4\Omega_0^2) \xi, \quad (25)$$

$$\frac{d\xi}{dr} = \frac{m^2}{\sigma_0^2 r^2} p + \left(\frac{2m}{\sigma_0 r} - \frac{1}{r} \right) \xi, \quad (26)$$

where $\sigma_0 = \lambda + m\mu$. The solution of these equations with the boundary condition (17) gives

$$\xi = \xi_* m r^{m-1}, \quad p = \xi_* \sigma_0 (\sigma_0 - 2\Omega_0) r^m, \quad (27)$$

where ξ_* is a constant that can be chosen arbitrarily.

We will analyze the cases that correspond to $m \geq 2$. The axisymmetric mode $m=0$ has been investigated by Howard.¹⁰ When $m=1$, no nontrivial solutions exist that satisfy both Eqs. (14) and (15) and the condition of zero velocity at the origin. Therefore, one can suggest that the $m=1$ mode is not realized in the basic vortex flow under consideration.

The swirl velocity decays and other parameters approach constant values at infinity exponentially fast as $r \rightarrow +\infty$, and therefore the eigenvalue equations can be asymptotically written as one equation for the pressure amplitude $p(r)$:

$$r^2 \frac{d^2 p}{dr^2} + r \frac{dp}{dr} + \left(\frac{\lambda^2}{C_\infty^2} r^2 - m^2 \right) p = 0. \quad (28)$$

The solution to this equation that satisfies Eq. (18) is the Hankel function $H_m^{(2)}$ (e.g., see Abramowitz and Stegun²¹), which represents an outward-going wave at infinity. Here we consider only the eigenvalues that have a negative imaginary part, $\text{Im}(\lambda) < 0$. For complex conjugate eigenvalues with $\text{Im}(\lambda) > 0$, corresponding temporally decaying modes, the solution is given by the Hankel function $H_m^{(1)}$, which describes inward-going waves.

The asymptotic solution for $r \rightarrow +\infty$ yields

$$p(r) = p_* H_m^{(2)}(\zeta), \quad (29)$$

$$\xi(r) = \frac{p_*}{\lambda C_{inf}} \left[H_{m-1}^{(2)}(\zeta) - \frac{m}{\zeta} H_m^{(2)}(\zeta) \right],$$

where $\zeta = \lambda r / C_{inf}$ and p_* is an unknown constant, which depends on the choice of the constant ξ_* in the asymptotic solution for $r \rightarrow 0$. Eliminating p_* yields the following asymptotic relation between ξ and p amplitudes when $r \rightarrow +\infty$:

$$\lambda C_{inf} H_m^{(2)}(\zeta) \xi(r) = \left[H_{m-1}^{(2)}(\zeta) - \frac{m}{\zeta} H_m^{(2)}(\zeta) \right] p(r). \quad (30)$$

The calculation of the complex eigenvalue λ can be then fulfilled by solving Eqs. (14) and (15) as an initial-value problem with the initial data in the form of Eq. (27) applied at some small $r=r_{00}$. The iteration parameter is the eigenvalue λ which is varied until the solution satisfies the asymptotic relation given by Eq. (30) at a large $r=r_{inf}$.

This approach is realized with the use of the MATLAB, a software for mathematical computing.²² The calculation is performed with the MATLABS program *bvp4c* that implements a collocation method for the solution of a set of differential equations $d\vec{y}/dx = \vec{f}(x, \vec{y}, \vec{p})$ on an interval $a \leq x \leq b$, subject to general, two-point boundary conditions $\vec{g}(\vec{y}(a), \vec{y}(b), \vec{p}) = 0$, where \vec{p} is a vector of unknown parameters. The *bvp4c* solution gives the vector \vec{p} and a continuous function $\psi(x)$, which is a cubic polynomial on each subinterval of a computational mesh and approximates the solution to the boundary-value problem $\vec{y}(x)$ with the fourth order of accuracy. We apply the *bvp4c* solver to a sequence of problems given by Eqs. (14), (15), (17), and (30) on intervals $[r_{00}, r_{inf}]$ for different, gradually increasing values of r_{inf} . The calculation is started with $r_{inf}=3$. The convergence of λ is typically achieved at the value of $r_{inf} \approx 5$ for the cases to be considered.

D. Results of the normal mode stability analysis

In this section we discuss results of the stability analysis for various cases of the basic flow. In the vortex model assumed in the present paper, the flow is defined by three parameters: μ that characterizes the vortex intensity, and θ and α that model the entropy distribution [see Eqs. (21) and (22)]. The case $\theta < 0$ corresponds to an excess of entropy in the vortex core. The entropy decreases with the distance

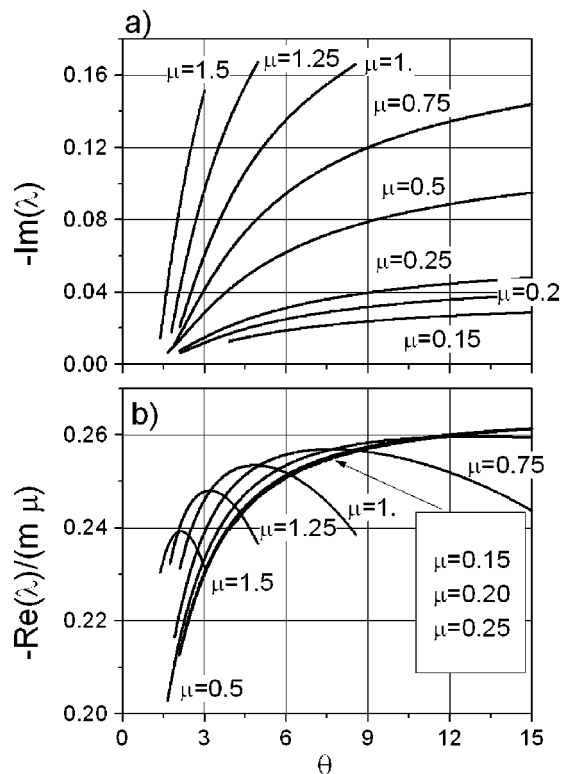


FIG. 1. (a) Growth rate and (b) azimuthal phase velocity vs θ for various values of the vortex intensity.

from the vortex center, fast approaching to its value at infinity. This situation here referred to as “overentropic vortex” can be found, for example, in rolled-up vortices in mixing layers and wake flows.¹² The opposite situation, when $\theta > 0$, is referred to as underentropic vortex. In this case, a shortage of entropy is in the core so that the entropy increases as we move far from the center. The homentropic vortex corresponds to $\theta = 0$. The parameter α relates to the inflection point in the entropy profile r_{ip} , which is inversely proportional to $\sqrt{\alpha}$, $r_{ip} \sim 1/\sqrt{\alpha}$.

1. Stability of underentropic vortex flows

Solution of the eigenvalue problem for the mode $m=2$ shows that underentropic vortices with a sufficiently large value of θ are unstable for the whole region of feasible vortex intensities. For $\alpha=0.5$ and various values of μ , the variations with θ of the growth rate λ_i and the azimuthal phase velocity normalized by μ , $\lambda_r/m/\mu$ are shown in Figs. 1(a) and 1(b), respectively. As seen from this figure, the instability becomes weaker (i.e., the growth rate gradually decreases approaching zero) as θ decreases for all considered values of μ . This trend is clearly discernible in the plots. Separately in Fig. 2, we show the behavior of the growth rate as it approaches zero [a closeup view of Fig. 1(a) around the origin]. One can see that the marginal state $\lambda_i=0$ when the vortex becomes neutrally stable is reached at a certain nonzero θ that depends on the vortex intensity. These marginal values are also listed in Table I.

For weak vortices, the phase velocity is well scaled by the maximal swirl velocity μ . This is clearly seen in Fig.

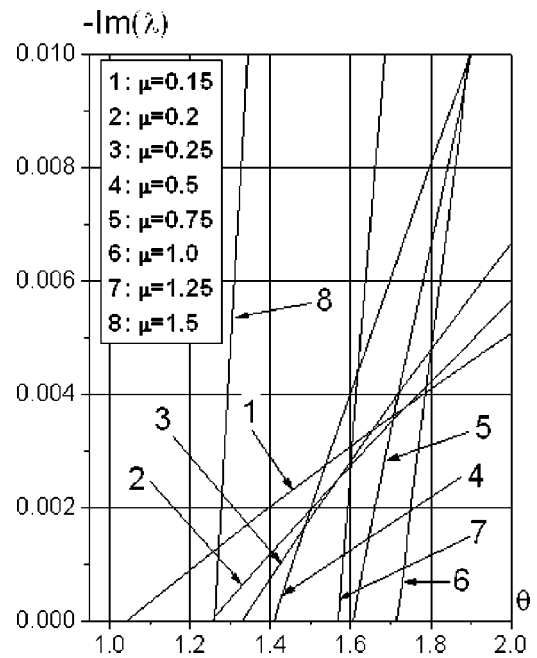


FIG. 2. Behavior of the growth rate vs θ in the vicinity of the marginal state for various values of the vortex intensity.

1(b): The curves representing the phase velocity normalized by μ are almost collapsed for values of μ less than 0.5.

Figure 3 shows the behavior of λ with the vortex intensity for various values of θ . These results also correspond to $\alpha=0.5$ and $m=2$. As seen in Fig. 3(a), the growth rate is monotonically decreased as the vortex intensity weakens. It should be also noted that for a large entropy stratification with $\theta \geq 2$, the marginal state begins right at $\mu=0$, i.e., vortices of any nonzero intensity are unstable. On the other hand, weakly stratified vortices with $\theta < 2$ become neutrally stable even at some nonzero values of μ .

The range of variation of the phase frequency, which is shown in Fig. 3(b), does not change very much with θ . The curves are nearly aligned with a straight line $\mu = -2\lambda_r$; it means that the azimuthal phase velocity is well scaled by the swirl velocity of the basic flow and amounts approximately to a quarter of its maximal value.

2. Stability of overentropic vortex flows

Analysis of overentropic vortices shows that they will also be unstable with respect to the $m=2$ normal mode disturbances if the average gradient of entropy in the basic flow is sufficiently large. We show the real and imaginary parts of the complex eigenvalue λ in Figs. 4(a) and 4(b), respectively, for $m=2$ and $\alpha=0.5$. The real part is normalized here with the maximal swirl velocity of the basic flow μ . The distributions are given versus the factor of entropy stratification θ for different μ . The cases displayed correspond to vortex velocities ranging from zero to a moderately large value $\mu=2.5$.

For this region, the growth rate $-\lambda_i$ falls to zero nonlinearly as the stratification factor decreases. As seen from Fig. 4(a), the stronger the vortex is the faster it approaches the marginal state $\lambda_i=0$ as the entropy stratification weakens. The marginal value of θ , for which the vortex becomes neu-

TABLE I. Marginal values of θ : $m=2$ mode, underentropic vortex, $\alpha=0.5$.

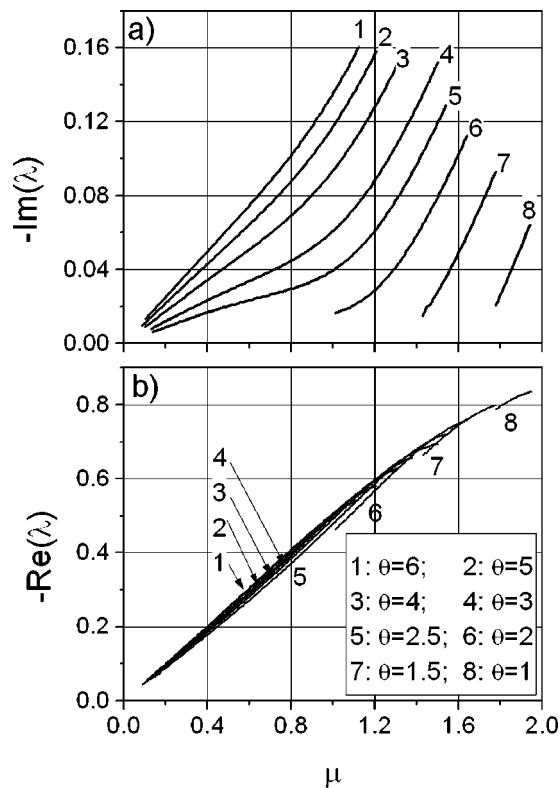
μ	0.15	0.2	0.25	0.5	0.75	1.0	1.25	1.5
θ	1.05	1.25	1.33	1.42	1.58	1.72	1.58	1.26

trally stable, is typically negative for large values of μ in the range considered. With decreasing μ , the marginal value moves towards zero that is reached by approximately $\mu = 1.25$. The weaker vortices remain unstable for all negative θ and the marginal state begins at a positive θ , i.e., in the underentropic region, only.

The normalized azimuthal phase frequency, λ_r/μ , does not change very much with both θ and μ , as can be seen from Fig. 4(b). The dependence on θ is almost linear; the phase velocity, λ_r/m , is slightly increased as the factor of entropy stratification tends to zero, ranging from 10% to 15% of the maximal swirl velocity.

The case of a stronger vortex with $\mu \geq 2.5$ is displayed in Fig. 5, where the growth rate is plotted versus θ for various μ . It appears from these plots that the marginal state is not achieved for vortices with the intensity larger than 2.75. These vortices remain unstable for all feasible θ ranged from -1 to the critical value θ_{ev} that corresponds to the vortex evacuated its center.

Near the evacuation regime, both underentropic and overentropic flows are found to be unstable. In Fig. 6 we show the eigenfrequency of the $m=2$ mode along a curve $\mu=0.95\mu_{ev}(\theta)$ [where μ_{ev} is defined by the equality in Eq. (24)] computed for $\alpha=0.5$. One can see that the growth rate

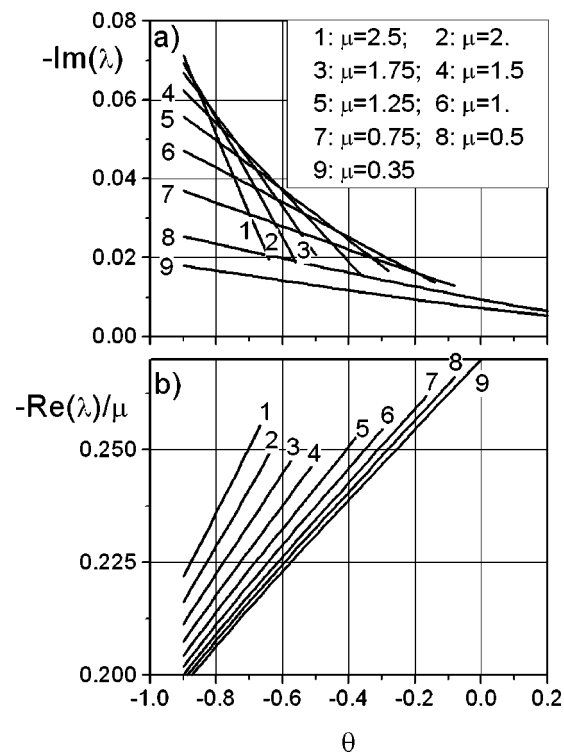
FIG. 3. (a) Growth rate and (b) azimuthal phase frequency vs vortex intensity for various values of θ .

decreases with increasing θ in the overentropic region. However, the marginal state is not reached; the growth rate acquires the minimum and then increases, tending to a constant for large θ in the underentropic region.

The marginal curve in the μ - θ plane, which defines the region of neutral stability, can be derived from the foregoing data. This curve is shown in Fig. 7 for the $m=2$ mode and $\alpha=0.5$. It bounds an area where the vortex is neutrally stable. As it was already mentioned, the stability is lost when the entropy stratification becomes sufficiently large and also near the evacuation region. An interesting fact is that the flow ceases to be stable also when the vortex weakens, i.e., μ decreases to a certain limit. In particular, homentropic vortices ($\theta=0$) are stable for $\mu \geq 1.25$ (except for a narrow band in the vicinity of the evacuation curve). More weaker vortices turn to be unstable, as seen from Fig. 7. It should be noted that this contrasts with the case of a Gaussian vorticity profile vortex, which was shown to be neutrally stable for all vortex intensities.¹²

3. Effect of α parameter

The entropy profile is modeled by means of two parameters: θ that characterizes the deviation from the homentropic distribution and α that defines the extent of the entropy core.

FIG. 4. Eigenfrequency vs entropy stratification parameter θ for overentropic vortices.

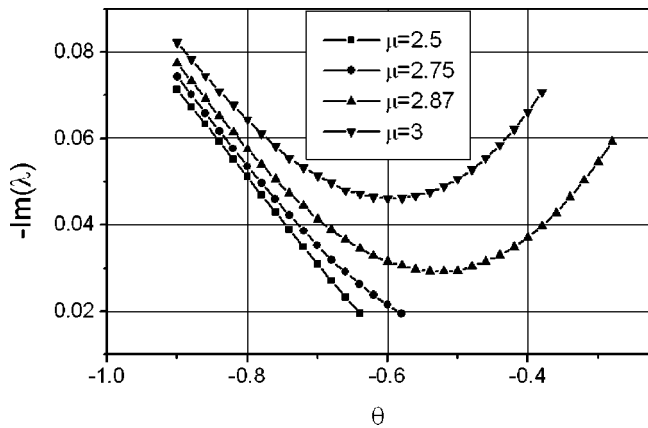


FIG. 5. Growth rate vs θ for overentropic strong vortices.

The foregoing results correspond to the case $\alpha=0.5$, when the entropy core nearly matches the vortex size. This section addresses the effect of the extent of the entropy core on the vortex instability properties, i.e., the effect of the α parameter.

Figure 8 shows the $m=2$ eigenfrequency against α parameter for the underentropic vortex with $\theta=3$ under various flow regimes (intensities). When α is small, which means that the entropy core much exceeds the vortex core, the flow is weakly unstable. The growth rate [Fig. 8(a)] approaches zero as α vanishes because the vortex acquires an homentropic distribution, under which it was shown to be stable. With reducing the size of the entropy core, i.e., increasing α , the growth rate is first increased and reaches the maximum. This corresponds to the situation when the maximal entropy stratification falls within the vortex periphery, where the flow velocity rapidly drops from its maximum to zero. Further increase in α weakens the instability, and low intensity flows ($\mu=0.3, 0.8$) become even neutrally stable, as seen in Fig. 8(a). The instability arises again becoming stronger for sufficiently large values of α , which corresponds to a region of entropy changemostly localized inside the vortex core ($r \leq 1$).

The phase frequency normalized with μ is shown in Fig. 8(b). One can see that the phase velocity, λ_i/m , is well scaled

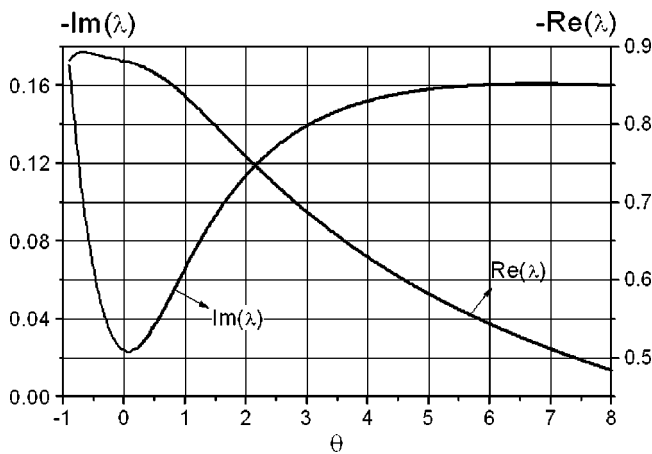


FIG. 6. Eigenfrequency vs θ for the vortex flow near the evacuation regime.

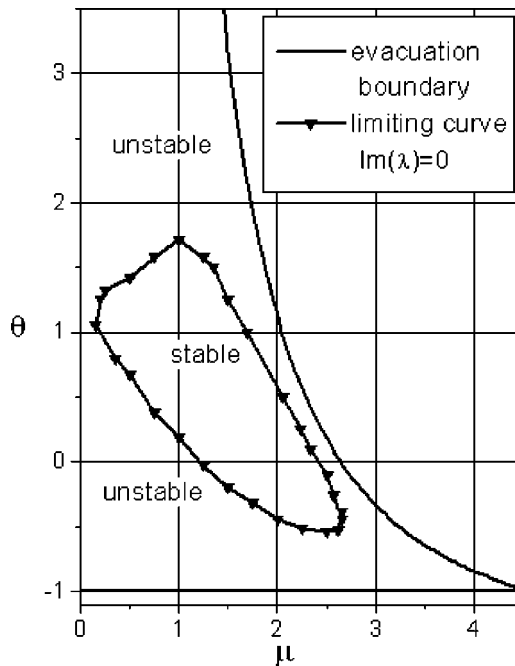


FIG. 7. Marginal curve in the μ - θ plane for stability of the $m=2$ mode for $\alpha=0.5$.

by the vortex intensity. With increasing α , the phase velocity is gradually rising but does not exceed the maximal swirl velocity.

The case of an overentropic vortex is shown in Fig. 9. The growth rate is plotted as a function of α for $\theta=-0.5$, $m=2$, and two velocity regimes $\mu=0.3$ and $\mu=1.3$. The be-

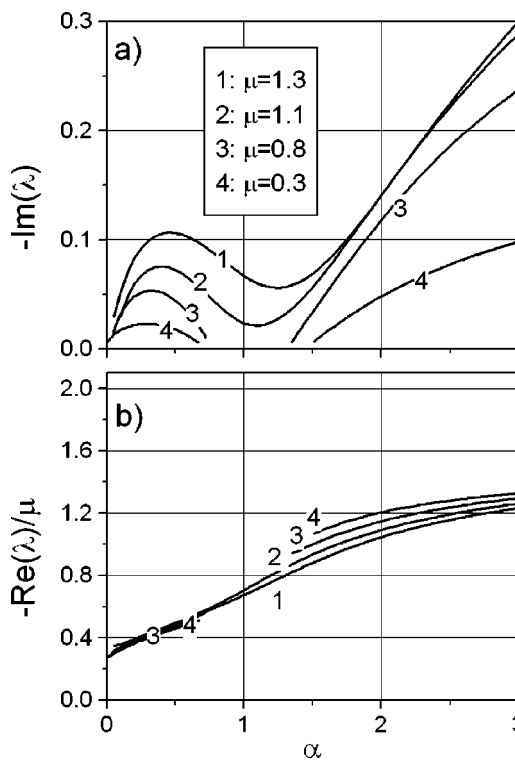


FIG. 8. (a) Growth rate and (b) azimuthal phase velocity against α parameter for $\theta=3$ and various vortex intensities.

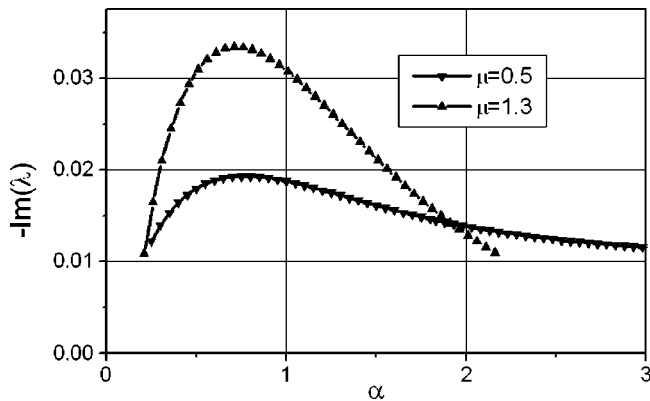


FIG. 9. Growth rate vs α parameter for $\theta=-0.5$.

havior of the growth rate is quite different from that in the foregoing underentropic case. The growth rate peaks at about $\alpha=0.75$, which corresponds to a profile of entropy with the inflection point located in the vortex core at about $r=0.5$. Increasing α , i.e., reducing of the entropy core, weakens the instability. However, unlike the underentropic case, the flow remains unstable; any stable regimes are not found in all range of the α variation.

4. Instability of high-order modes

Results related to the stability of high-order azimuthal modes are presented in this section for the basic flow represented by an underentropic vortex. In calculating a high-order mode (say $m=3$), we start with the solution for the $m=2$ mode as an initial approximation. Then the eigenvalue problem is successively calculated assuming that m is not an integer, but a real, which is gradually varying from one calculation to another with a small step Δm until it takes the higher integer value, $m=3, 4$, etc. In these calculations, the previously computed eigenfrequency and eigenfunctions make an initial guess for the subsequent problem.

Comparison between the $m=2$ and $m=3$ solutions is presented in Fig. 10. The phase velocity [Fig. 10(a)] and the growth rate [Fig. 10(b)] are plotted versus the vortex intensity for a profile of entropy with $\alpha=3$ under three values of θ . The number on the plots indicates the order of mode. The growth rates do not differ very much for low intensity flows. However, a noticeable difference is found at higher values of intensity, near the evacuation regime, where the $m=3$ mode becomes more unstable than the $m=2$ mode. The phase velocities show a minor discrepancy; the phase velocity of the higher mode is about 10% larger than that of the $m=2$ mode in all range of the intensity variation as seen from Fig. 10(a).

In Fig. 11 the effect of the core size on stability of higher-order normal modes ($m=3, 4$) is shown for two velocity regimes, $\mu=0.3$ and $\mu=1.3$. The results for the $m=2$ mode are also included in this figure for comparison. For sufficiently large α (the entropy core is localized inside the vortex core very near to its center) all modes $m=2, 3$, and 4 are unstable. As α decreases (the entropy core enlarges) growth rates of all modes decline, with the rate of decline being faster for higher-order modes. When the inflection point of the entropy profile reaches a location near $r=1$, first

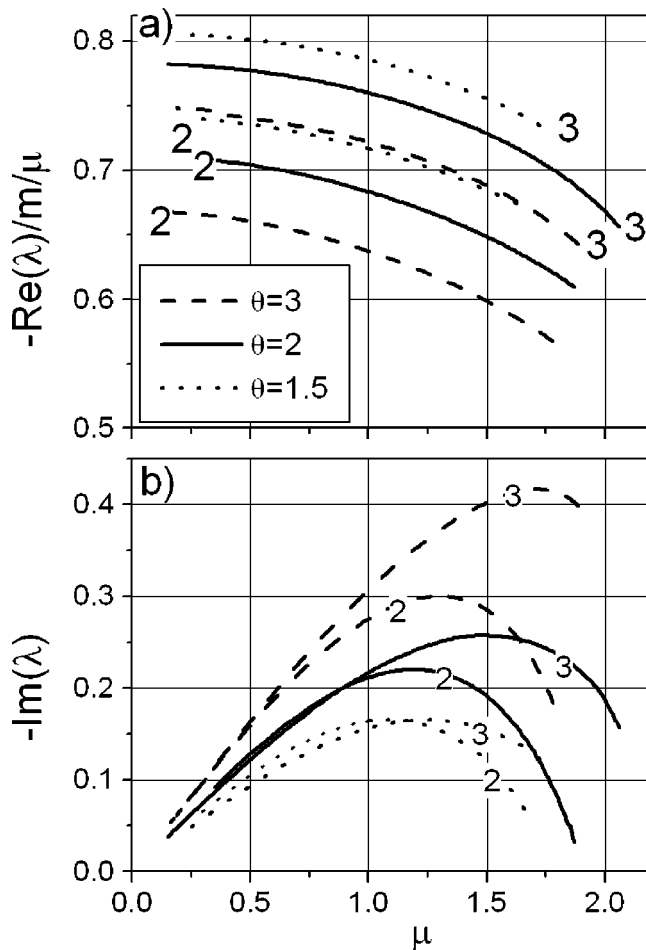


FIG. 10. (a) Phase velocity and (b) growth rate against μ for $m=2$ and $m=3$ modes and various θ .

the $m=4$ and then the $m=3$ mode is stabilized. Further enlargement of the entropy core does not affect the stability of these modes in contrast to the $m=2$ mode, which becomes unstable again when the core expands beyond the vortex core by its periphery.

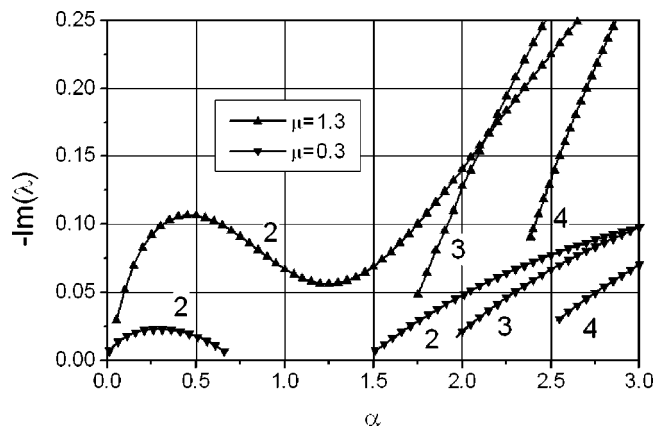


FIG. 11. Growth rate of $m=2, 3, 4$ modes vs α parameter.

III. EXCITING OF INSTABILITY BY SOUND

The foregoing linear-stability analysis shows the existence of unstable normal modes of small disturbances developing against the background of the basic vortex flow. In this section we consider an example of the situation where these modes can be excited, namely, the scattering of a plane sound wave by the vortex flow.

The scattering of sound by a vortex is one of benchmark problems in aeroacoustics. It has been intensively investigated by many researches (as latest publications on this subject see Colonius *et al.*²³ and Ford and Llewellyn Smith²⁴). All these studies were mainly addressed basic characteristics of the scattered sound field. However, as unstable modes exist, one can expect excitation of these modes in the sound scattering process, which must greatly affect the resultant scattered field. To this end, we will study the scattering problem with the purpose that is twofold: to show that the scattered field is really destabilized in the process of sound scattering and to compare basic characteristics of this instability, such as the growth rate and azimuthal phase velocity, with those predicted by the linear-stability analysis.

A. Solution method

The scattering problem is investigated by solving the LEE numerically. The LEE is a commonly used model for aeroacoustic applications (e.g., see Mankbadi *et al.*²⁵ and Bailly *et al.*²⁶). In this model, the fluid flow is decomposed into a base flow and a field of disturbances whose magnitude is assumed to be much smaller than that of the basic flow. The latter is assumed to be prescribed and not modified by disturbances, whereas the evolution of the disturbance field depends on the basic flow and is determined by linearized equations.

The method used in the present study differs from the conventional LEE approach. The main distinctive feature is that the linearization is performed for the discretized Euler equations rather than the differential ones. This allows us to express the resultant discretized equations for disturbances in the conservative form. (Note that the conventional LEE are nonconservative, and therefore special attention should be given to numerical algorithms to handle wave-type solutions correctly, as was pointed out by Viswanathan and Sankar.²⁷) Some elements of the method are described below. For further details, the reader is referred to Men'shov and Nakamura.²⁸

The conservative form of the discretized equations for the evolution of small disturbances against the background of a basic nonuniform flow field is given by

$$\omega_i \frac{d\hat{\mathbf{q}}_i}{dt} + \sum_{\sigma} s_{\sigma} T_{\sigma}^{-1} \hat{\mathbf{F}}_{\sigma} = 0, \quad (31)$$

where the subscript i denotes the order number of the computational cell, the subscript σ denotes the cell interface that borders the i th cell, ω is the volume, s is the area, and T_{σ} is the transforming matrix defined by the components of unit vectors of the local orthonormal basis relevant to the interface. Moreover, \mathbf{q} represents the vector of conservative vari-

ables, \mathbf{F} represents the relevant flux vector, the hat denotes disturbance values, while the bar will denote basic flow values.

The key point of the method is the approximation of the cell interface disturbance flux $\hat{\mathbf{F}}_{\sigma}$ that depends on both the basic flow and the disturbance field, $\hat{\mathbf{F}}_{\sigma} = \hat{\mathbf{F}}_{\sigma}(\hat{\mathbf{q}}, \bar{\mathbf{q}})$. We treat it from the point of view of the Godunov approach²⁹ as the flux that steams at an interface due to interaction between two parcels of the disturbance field neighboring this interface. The interaction can be mathematically described in terms of the solution to the variational Riemann problem²⁸ (VRP) that is stated as the problem on the first variation of the conventional Riemann problem solution with respect to variations in initial data. The latter admits the analytical solution, which can be used for the flux approximation.

By introducing $\mathbf{Q} = \mathbf{T}_{\sigma} \mathbf{q}$, this flux is obtained in terms of the solution to the VRP as follows:

$$\hat{\mathbf{F}}_{\sigma}(\bar{\mathbf{q}}, \hat{\mathbf{q}}) = A(\bar{\mathbf{Q}}_{\sigma}^R) \hat{\mathbf{Q}}_{\sigma}^R, \quad (32)$$

where $A(\mathbf{Q}) = \partial \mathbf{F} / \partial \mathbf{Q}$ is the Jacobian matrix of the local one-dimensional inviscid flux, $\bar{\mathbf{Q}}_{\sigma}^R = \bar{\mathbf{Q}}_{\sigma}^R(\bar{\mathbf{Q}}_i^{\sigma}, \bar{\mathbf{Q}}_{\sigma(i)}^{\sigma})$ is the solution to the conventional Riemann problem stated for the cell interface σ treated as a surface of discontinuity, and $\bar{\mathbf{Q}}_i^{\sigma}$ and $\bar{\mathbf{Q}}_{\sigma(i)}^{\sigma}$ as initial values on the left- and right-hand sides, respectively. Here, the subscript $\sigma(i)$ denotes the order number of the cell that adjoins the i th cell by the σ th cell interface. The superscript σ indicates the value of a variable at the center of the cell interface.

The vector $\hat{\mathbf{Q}}_{\sigma}^R$ in Eq. (32) is the solution to the VRP, which yields the variation of the Riemann problem solution due to the presence of the disturbance field in the two neighboring cells. This vector is expressed in terms of variational matrices M_i and $M_{\sigma(i)}$,

$$\hat{\mathbf{Q}}_{\sigma}^R = M_i \hat{\mathbf{Q}}_i^{\sigma} + M_{\sigma(i)} \hat{\mathbf{Q}}_{\sigma(i)}^{\sigma}. \quad (33)$$

These matrices can be found analytically (for details, the reader is referred to Men'shov and Nakamura,³⁰ where exact analytical formulas are also presented).

The superscript σ in Eq. (33) means that the vectors of disturbance parameters are evaluated at the middle point of the interface. A first-order scheme is obtained, if a constant function is used to approximate the distribution of disturbances within the computational cell: $\hat{\mathbf{Q}}_i^{\sigma} = \hat{\mathbf{Q}}_i$. To enhance the accuracy of the method, the disturbance vector can be interpolated via the MUSCL approach.³¹ This leads to the σ values given by

$$\hat{\mathbf{q}}_i^{\sigma} = \hat{\mathbf{q}}_i + 0.5 \delta^{-} [1 - k(\delta^{-})] \Delta_i^{-} + 0.5 \delta^{-} [1 + k(\delta^{-})] (\hat{\mathbf{q}}_{\sigma(i)} - \hat{\mathbf{q}}_i), \quad (34)$$

$$\hat{\mathbf{q}}_{\sigma(i)}^{\sigma} = \hat{\mathbf{q}}_{\sigma(i)} - 0.5 \delta^{+} [1 - k(\delta^{+})] \Delta_{\sigma(i)}^{+} + 0.5 \delta^{+} [1 + k(\delta^{+})] (\hat{\mathbf{q}}_i - \hat{\mathbf{q}}_{\sigma(i)}) \quad (35)$$

where $\delta^{-} = |\vec{r}_{i,\sigma}| / (|\vec{r}_{i,\sigma}| + |\vec{r}_{\sigma(i),\sigma}|)$, $\delta^{+} = 1 - \delta^{-}$, and $\vec{r}_{i,\sigma}$ is the radius vector from the cell center to the interface center. The forward and backward difference operators are given by

$$\Delta_i^- = \frac{2}{\delta} (\vec{\nabla} \mathbf{q})_i \vec{r}_{i,\sigma} - (\hat{\mathbf{q}}_{\sigma(i)} - \hat{\mathbf{q}}_i), \quad (36)$$

$$\Delta_{\sigma(i)}^+ = -\frac{2}{\delta^+} (\vec{\nabla} \mathbf{q})_{\sigma(i)} \vec{r}_{\sigma(i),\sigma} - (\hat{\mathbf{q}}_{\sigma(i)} - \hat{\mathbf{q}}_i). \quad (37)$$

The gradient in these equations is computed with the method of least squares.

The function $k(\delta)$ controls a family of difference schemes in the foregoing interpolation. Thus, on structured grids, taking $k=-1$ leads to a fully upwind scheme, $k=1$ corresponds to central differencing, and $k=0$ yields a scheme by Fromm.³² The choice $k=(12\delta^2-1)/(12\delta)$ leads to an upwind-biased third-order scheme. Strictly speaking, third-order accuracy is achieved only for one-dimensional problems. Nevertheless, we use this option for the two-dimensional calculations presented below.

With the foregoing remarks, Eq. (31) can be written as

$$\frac{d\hat{\mathbf{q}}_i}{dt} = \mathbf{R}_i(\hat{\mathbf{q}}), \quad (38)$$

with

$$\mathbf{R}_i(\hat{\mathbf{q}}) = -\frac{1}{\omega_i} \sum_{\sigma} s_{\sigma} T_{\sigma}^{-1} A(\bar{\mathbf{Q}}_{\sigma}^R) [M_i T_{\sigma} \hat{\mathbf{q}}_i^{\sigma} + M_{\sigma(i)} T_{\sigma} \hat{\mathbf{q}}_{\sigma(i)}^{\sigma}], \quad (39)$$

which can then be integrated numerically by a third-order accurate Runge–Kutta method.³³ The scheme obtained is stable under the conventional CFL condition based on the largest absolute wave speed of the basic flow.

B. Validation of the numerical method

The foregoing numerical method has been verified by some test calculations in our previous work.³⁴ In this section we apply it to compute the scattered sound resulted from the incidence of sound waves on an isolated vortex. The computational domain is a square, the middle point of which matches the center of the vortex. A plane sound wave is emitted from the left side of the domain towards the vortex. The scattered field is obtained by subtracting the acoustic field computed in the gas at rest from that computed in the presence of the vortex flow.

The generation of incident waves is modeled by setting the disturbance vector at the left-hand boundary of the computational domain in the form of a plane monochromatic sound wave. The bottom, top, and right-hand boundaries are treated with nonreflecting boundary conditions.³⁴ The computational grid consists of 271 cells in each direction; the extent of the computational domain is 20 radii of the vortex core. The basic flow is defined by the distributions given by Eqs. (21) and (22). There are no disturbances presented in the computational domain at initial.

To validate the numerical method, we first calculated the scattered field in the case of a low-intensity homentropic vortex ($\theta=0$). This case has been intensively studied during the last twenty years (e.g., see Ford and Llewellyn Smith²⁴

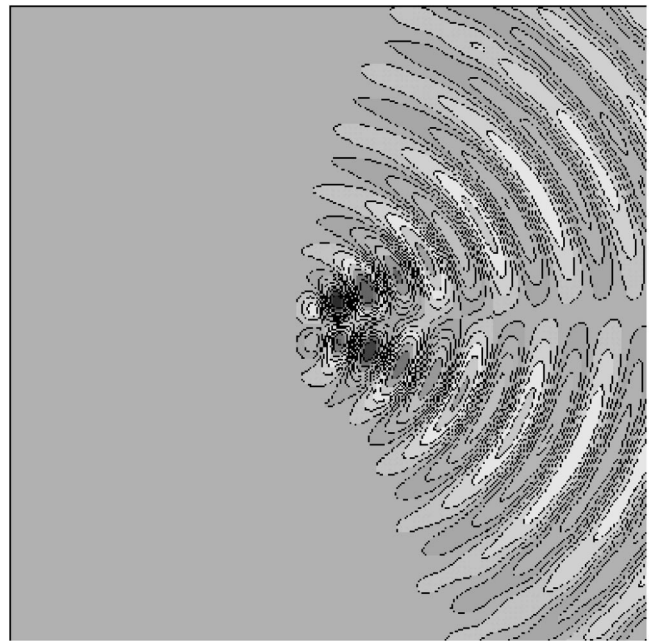


FIG. 12. Instantaneous pressure contours of the scattered field for $\mu=0.15$ and $\delta=4$.

and references therein), and therefore many theoretical and numerical results are available for comparison.

Figure 12 shows instantaneous pressure contours of the scattered field for the intensity $\mu=0.15$ and $\delta=4$, where δ is the nondimensional wavelength of the incident wave. One can see that the forward scattering is much dominant over the backward one, with the maximum scattering being achieved in two directions that make angles of about $\pm 30^\circ$ with the direction of wave incidence. The root-mean-square pressure amplitude of the scattered waves p_{rms} is plotted as a function of the polar angle ϕ for various values of the radius r in Fig. 13. The pressure is normalized by the pressure amplitude of the incident wave p_0 and the factor $\sqrt{\lambda_s}/r$, where λ_s is the wavelength. According to the analysis given by Howe,³⁵ the scattering amplitude decays in the far field as $\sqrt{r^{-1}}$. This is also confirmed by the present calculations: The curves in Fig. 13 tend to collapse into a single curve as the ratio r/λ_s increases.

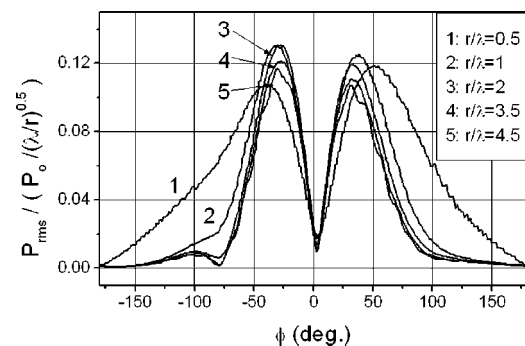


FIG. 13. Normalized root-mean-square pressure levels for $\mu=0.15$ and $\delta=4$.

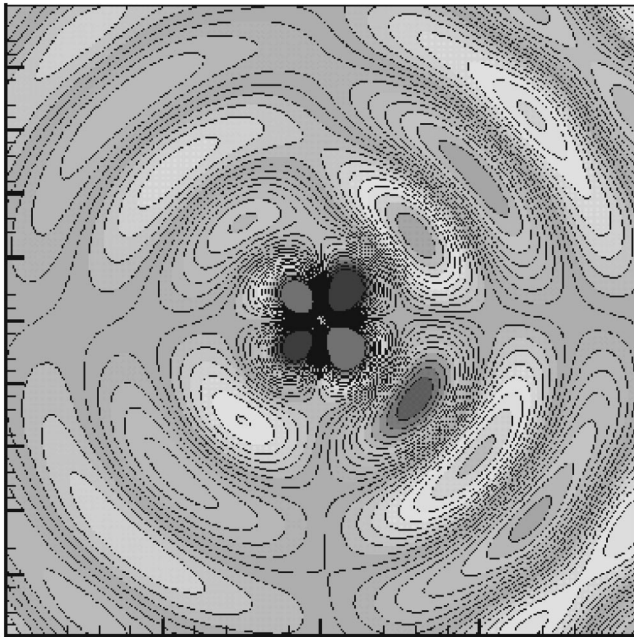


FIG. 14. Instantaneous contours of pressure in the scattered field for $\mu=0.15$ and $\delta=10$.

The wave pattern of the scattered field changes drastically, as the wavelength of the incident waves increases. The region where scattering waves travel extends toward the backward direction. The backscatter phenomenon is intensified and becomes comparable with the forward scattering. For low intensities, a far-field approximation of the scattered field can be analytically obtained for incident waves that have much longer wavelengths compared with the scale of the vortex. This is so called Born limit that was investigated by Fabricant.³⁶ According to this analysis, the scattering in the Born limit occurs in both forward and backward directions with a typical quadrupole directivity pattern.

The present LEE-based model also confirms the backscatter phenomenon. In Fig. 14 we show instantaneous pressure contours of the scattered waves under the conditions: $\mu=0.15$ and $\delta=10$. The scattered field directivity is evidently of the quadrupole type: the maximal scattering occurs at polar angles of about $\pm 40^\circ$ and $\pm 130^\circ$. The backward scattering is about one half the forward scattering, which well agrees with the far-field asymptotics.³⁶ The distribution of the root-mean-square pressure with ϕ is plotted in Fig. 15 for increasing values of the radius. The pressure is again normalized by the factor $\sqrt{\lambda_s}/r$ to validate the far field $1/\sqrt{r}$ scaling. One can see that all curves for radii larger than $r=2\lambda_s$ almost do not deviate from each other.

C. Instability of sound scattering in homentropic vortices

The simulation of sound scattering by weak vortices, as discussed in the foregoing, shows no instability of the scattered field; the computed disturbances were found to be strictly periodical in time, with the frequency exactly equal to that of incident waves. This seems to be contradictory to the linear-stability analysis that definitely predicts the exist-

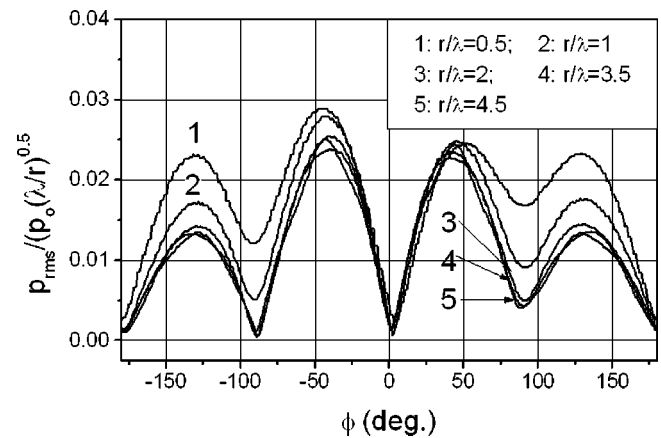


FIG. 15. Normalized root-mean-square pressure levels for $\mu=0.15$ and $\delta=10$.

tence of the $m=2$ unstable mode (see Fig. 7). In fact, there is no contradiction: the point is that the instability is very weak. The nondimensional growth rate is of the order of 10^{-3} for the case considered, and therefore the nondimensional time for the instability to develop sufficiently must be order of 10^3 or greater. The latter corresponds to about 20 vortex revolutions, but the foregoing simulation was executed for the time of about 30 incident wave periods, which corresponds to two and five vortex revolutions in the case $\delta=4$ and $\delta=10$, respectively. So the instability seems to be not able to develop during so little time period.

To verify this fact, long-time calculations have been carried out for a stronger homentropic vortex with $\mu=0.75$, for which the linear-stability analysis predicts the instability of the $m=2$ mode with a larger growth rate, $-\lambda_i=0.0106$, and the azimuthal phase velocity $-\lambda_r=0.2044$, as can be seen from Figs. 4(a) and 4(b), respectively. In these calculations the vortex is irradiated by sound waves with the wavelength $\delta=3$. The time behavior of two characteristics is investigated: the disturbance pressure at a reference point located right behind the vortex core ($r=2a$, $\phi=0$) and the disturbance pressure averaged over the region $V=\{r \leq 2a\}$ as

$$p_{av} = \sqrt{\frac{1}{|V|} \int_V \hat{p}^2 dV}. \quad (40)$$

The time histories of these two parameters, normalized with the amplitude of the incident wave, are shown in Figs. 16 and 17, respectively. One can see that no instability appears in the scattered field for a rather long time. Until the nondimensional time $t \approx 400$, which corresponds to about 50 vortex revolutions, the reference pressure exhibits strictly periodical behavior with the frequency that equals the frequency of incident sound; the average pressure p_{av} remains almost constant.

During the later time, one can see the sudden appearance of the instability, which manifests itself as fast amplification of the reference pressure amplitude. An increase in p_{av} is also observed, which acquires a nearly linear behavior with a slope of 0.01064 (in logarithmic scale), as indicated by Fig. 17. This slope exactly matches the growth rate given by the linear-stability analysis.

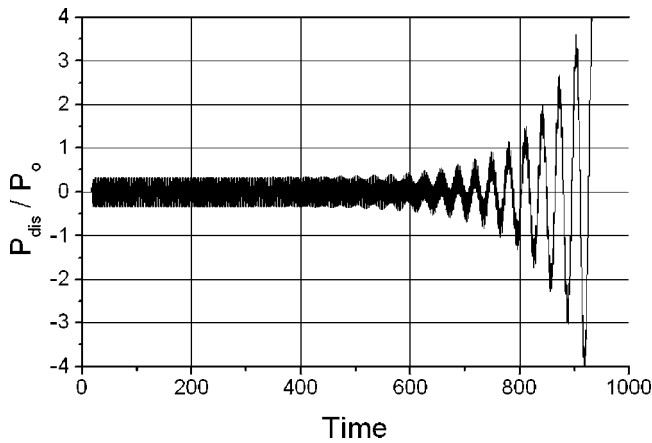


FIG. 16. Time history of the reference disturbance pressure for the homentropic vortex with $\mu=0.75$.

When performing FFT analysis for the reference pressure given in Fig. 16, the power spectrum is obtained, which is shown in Fig. 18. Two preferred frequencies exist in this spectrum: $\omega=2.4781$ that is the frequency of the incident wave and $\omega=0.2057$ that is related to the instability. The latter well agrees with the phase frequency of the $m=2$ normal mode ($-\lambda_r=0.2044$), as indicated by Fig. 18.

One can infer from the foregoing results that the instability of the sound scattering process is induced by the unstable $m=2$ normal mode, which results from the interaction of the incident acoustic waves with the basic vortex flow. This is also manifested by the pattern of the disturbance field after the instability has been excited. Figure 19 shows the instantaneous pressure field for the moment $t=932$, by which the vortex has executed about 100 revolutions. The pressure distribution is drastically modified in the vortex core and its periphery by this time, and acquires an azimuthally periodical structure that well responds to the $m=2$ normal mode. The disturbance velocity field becomes definitely rotational, represented by four symmetrically located swirls clearly discernible in Fig. 20. These swirls are located at the same polar angles as the peaks of pressure are. A higher pressure takes

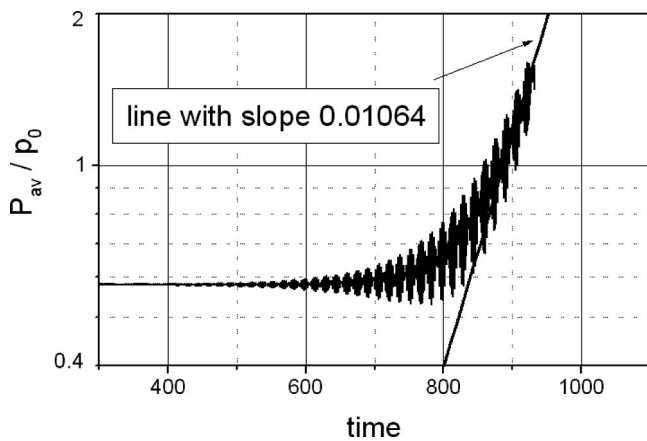


FIG. 17. Time history of the average disturbance pressure in the vortex with $\theta=0$ and $\mu=0.75$.

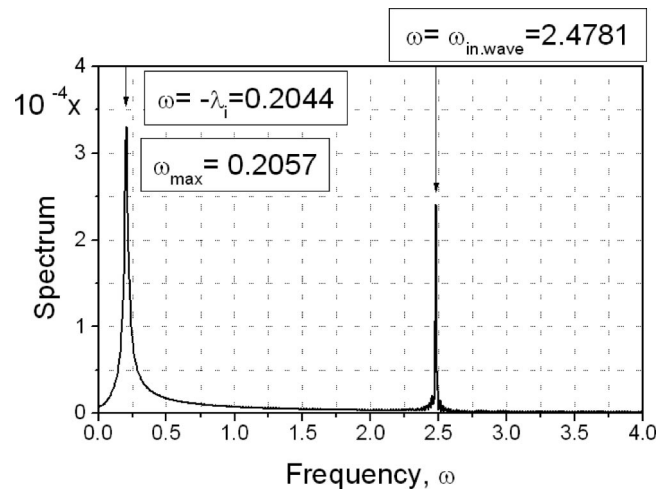


FIG. 18. Spectrum of the reference pressure for the vortex with $\theta=0$ and $\mu=0.75$.

place when the disturbance vortex and the basic vortex are corotating, while a lower pressure occurs in the counter-rotating vortices.

The linear-stability analysis shows that as the vortex intensity strengthens, the instability weakens, and eventually (at $\mu=1.25$) the basic flow changes into a neutrally stable state. Therefore one can also expect stabilization of the sound scattering process for a stronger vortex. To verify this fact, very-long-time calculations have been performed for an homentropic vortex of $\mu=1.75$ and $\delta=3$. Figure 21 shows the disturbance pressure at the moment $t=922.154$ when the vortex has been executed about 256 rotations. Incident waves are scattered by the vortex, with the disturbance field being amplified only approximately two times in the periphery of the core. The time history of the reference pressure shows exactly periodical behavior with no tendency for the ampli-

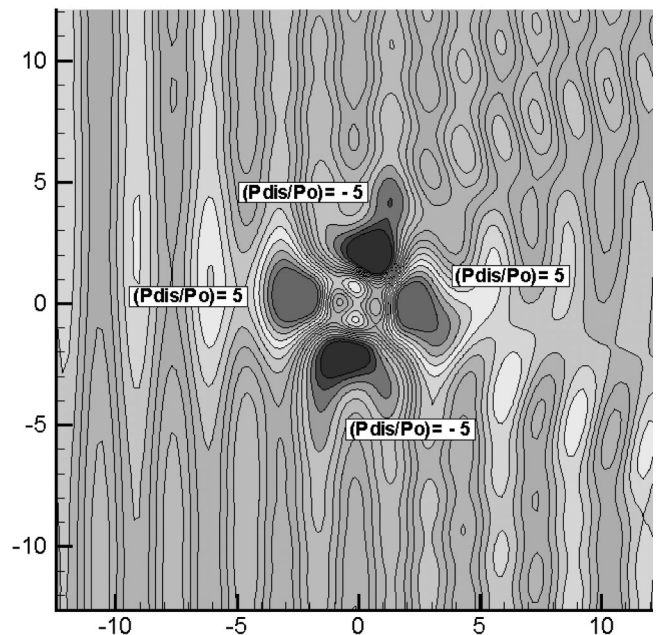


FIG. 19. Pressure disturbance field after the instability excitement.

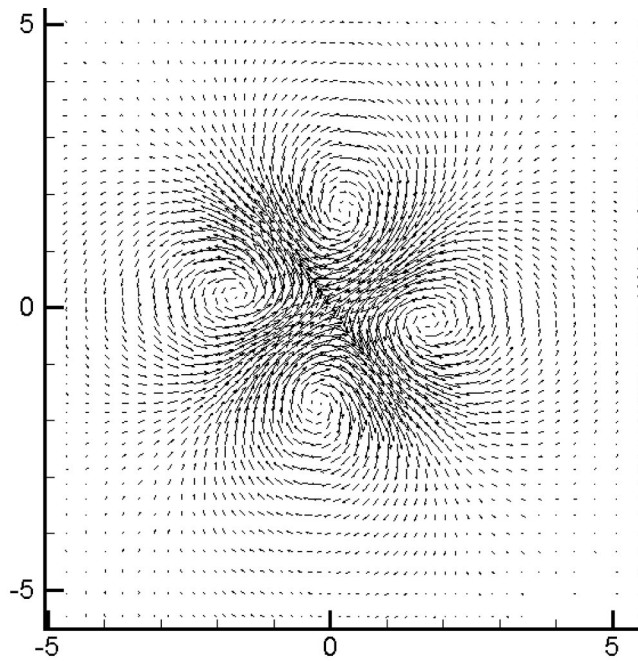


FIG. 20. Velocity disturbance field after the instability excitement.

tude to grow up. The result of the FFT analysis is displayed in Fig. 22. Only one frequency exists in the spectrum, $\omega = 2.4781$, which corresponds to the frequency of incident waves. Any other modes are not activated in this case. The velocity field does not reveal any peculiar vortical structures; the disturbance velocity field remains irrotational in contrast to the $\mu=0.75$ case.

It should also be noted that the entropy is not disturbed (the disturbance entropy equals zero exactly) when the homentropic vortex is irradiated by sound. This property is well supported by the present numerical results. Analysis of the disturbance of entropy in the foregoing two cases (unstable

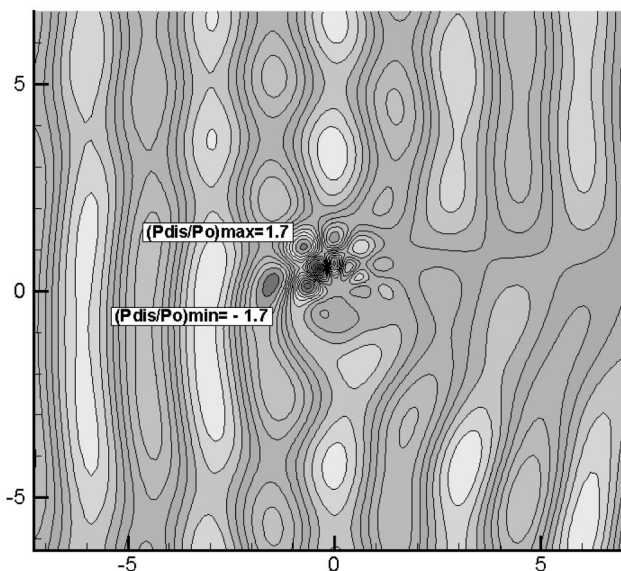


FIG. 21. Pressure disturbance field in the case when the instability is not excited: $\theta=0$ and $\mu=1.75$.

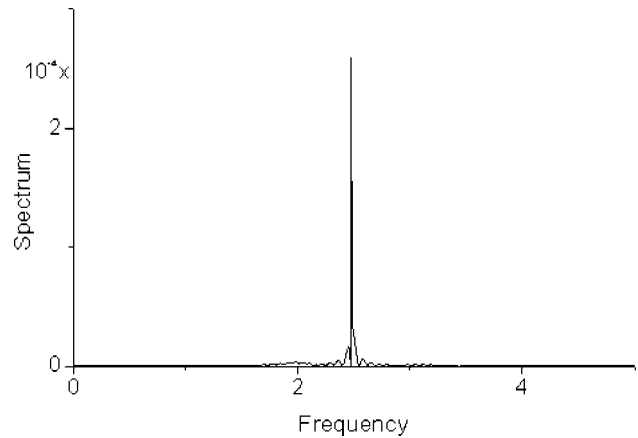


FIG. 22. Spectrum of the reference pressure for the vortex with $\theta=0$ and $\mu=1.75$.

and stable scattering) shows almost zero values throughout the computational domain; the maximal deviation of entropy disturbances from zero is about 10^{-6} , which is within the accuracy of the numerical method.

D. Instability of sound scattering in entropy-stratified vortices

This section addresses the sound scattering in nonhomotropic vortices. We consider the basic vortex that is defined by the intensity $\mu=1.3$ and the entropy profile of $\theta=3$ and $\alpha=0.5$. Under these conditions, the linear-stability analysis detects only one unstable mode— $m=2$ —with the temporal growth rate and azimuthal phase frequency given by $-\lambda_r=0.1063$ and $-\lambda_\theta=0.6409$, respectively (see Fig. 1). To simulate this instability, we consider the irradiation of the vortex by sound waves of $\delta=4$. The calculation results are presented below.

Figure 23 shows the time history of the average disturbance pressure in the vortex core p_{av} normalized with the amplitude of the incident wave. The instability is revealed by the moment $t \approx 50$ after the start of sound emission, when the vortex has made about ten revolutions. From this time, the average pressure begins to grow in magnitude with an expo-

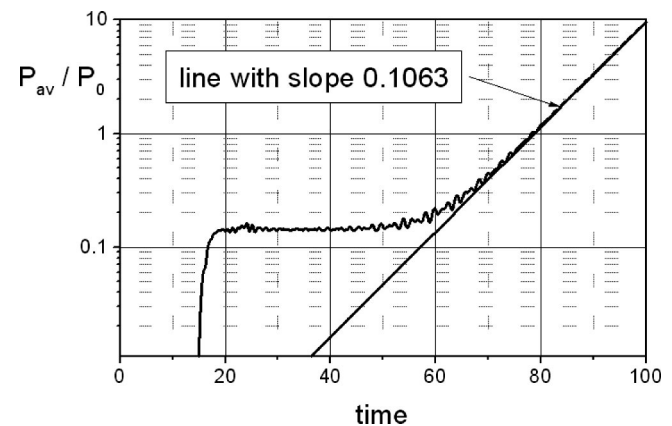


FIG. 23. Time history of p_{av} for an entropy-stratified vortex with $\mu=1.3$, $\theta=3$, and $\alpha=0.5$.

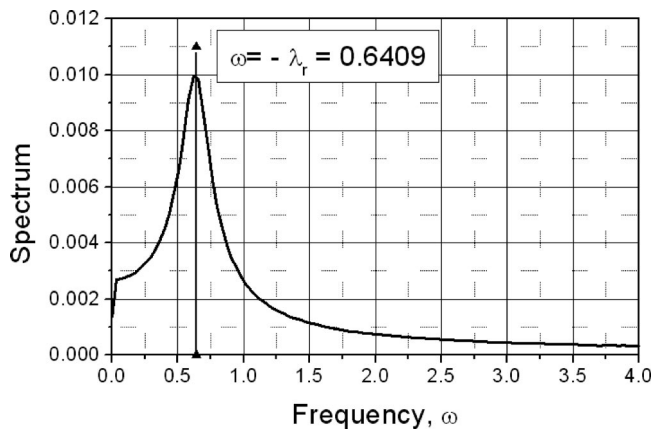


FIG. 24. Spectrum of the reference pressure for the entropy-stratified vortex with $\mu=1.3$, $\theta=3$, and $\alpha=0.5$.

nential rate: in the logarithmic scale, it acquires a linear dependence with respect to time, which matches a straight line with the tangent of the slope angle 0.1063, as seen in Fig. 23. The latter is well compared with the growth rate of the $m=2$ normal mode. Moreover, the spectrum of the reference disturbance pressure shows a dominant frequency which well coincides with the $m=2$ phase frequency, $\omega=-\lambda_r=0.6409$. This result is displayed in Fig. 24.

The foregoing data indicates that the instability in the sound scattering process is caused by the excitation of the unstable $m=2$ normal mode. As the instability progresses, the disturbance field acquires a typical four-leaved structure shown in Fig. 25, where instantaneous disturbance pressure contours are displayed for the moment $t=75$ (about 15 vortex revolutions). The disturbance velocity vector is shown in Fig. 26 for this moment along with the disturbance entropy field. One can see that a narrow circular entropy wave is induced

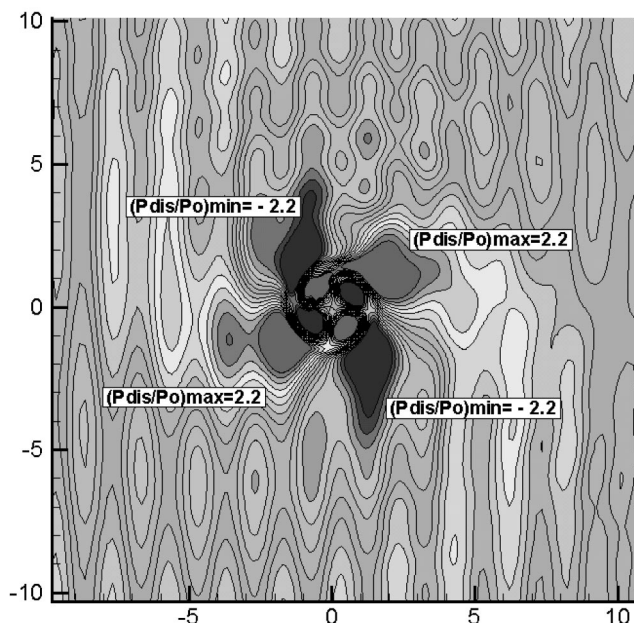


FIG. 25. Pressure disturbance field in the nonhomentropic vortex: excitation of the $m=2$ unstable normal mode.

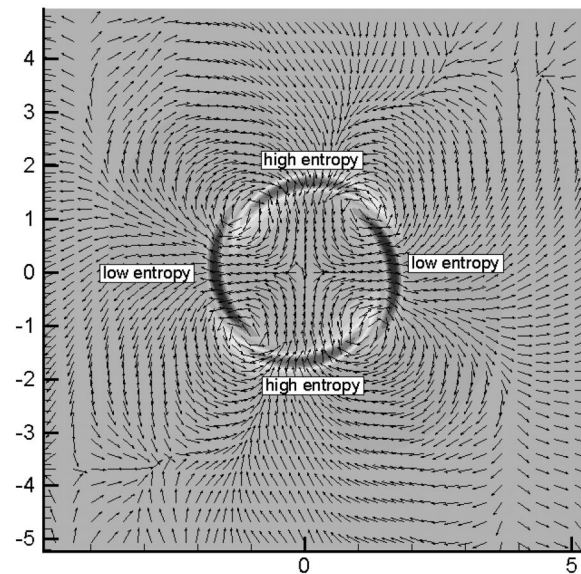


FIG. 26. Disturbance velocity vectors and entropy field in the nonhomentropic vortex ($\mu=1.3$, $\theta=3$, and $\alpha=0.5$).

in the vortex periphery region. Also, the velocity field becomes rotational and takes a regular structure that consists of four focus-type points located in the entropy wave and one saddle-type point in the vortex center.

IV. CONCLUSIONS

The normal mode linear analysis has been fulfilled to study the stability of two-dimensional compressible vortices. Unlike the previously studied vortices of one-signed vorticity and a finite circulation at infinity—the Rankine vortex of uniform vorticity jumping to zero at the core boundary¹¹ and vortices of a smoothed vorticity distribution¹²—we were concerned with isolated vortices where the vorticity core is surrounded by an annulus of opposite vorticity and the circulation almost vanishes at a finite distance from the core. The emphasis was done to the effect of entropy stratification (modeled by a two-parametric Gaussian-type profile) on stability properties. The major results and conclusions of this study are the following.

(1) Underentropic vortex (with entropy deficiency in the core) is unstable in all the regions of admissible vortex intensities when the deviation of entropy from the homentropic distribution defined by θ parameter, Eq. (22), is large enough. The instability weakens with decreasing θ and eventually the vortex goes into the neutrally stable state at some nonzero stratification. This behavior differs from that observed for vortices of one-signed finite vorticity distribution, which remain unstable under any entropy stratification.¹²

(2) Overentropic vortex (with entropy excess in the core) is found unstable under sufficiently large entropy stratification, with the instability getting also weaker as the entropy stratification is relaxed. Rather intense vortices (with the intensity μ greater 1.25 or so) are stabilized at some nonzero stratification, while more weak vortices remain unstable till

the homentropic condition ($\theta=0$). Note that for the one-signed vorticity vortex, the overentropic stratification is on the contrary a stabilizing factor.

(3) The effect of the entropy core size on the stability properties has been investigated. It was found that for the underentropic stratification, rather strong instability occurs when the entropy core is smaller than the vortex core. On the other hand, lessening the entropy core weakens the instability in the case of overentropic vortex.

(4) Very strong isolated vortices, near the evacuation regime, both underentropic and overentropic vortices were found unstable.

(5) The marginal curve that separates stable and unstable regions in the plane of vortex intensity μ and stratification parameter θ has been obtained for the most unstable $m=2$ mode. In particular, it shows that homentropic vortices of low intensities are unstable; the instability weakens as the intensity increases, and the homentropic vortex is eventually stabilized, remaining stable for higher intensities (except for a narrow band of instability near the evacuation regime). This contrasts with the vortex of one-signed Gaussian-distributed vorticity,¹² which was shown to be neutrally stable under all intensities.

(6) It has also been shown that unstable normal modes can be induced in the scattered field when sound waves irradiate the vortex. The sound scattering problem has been numerically studied with a discrete LEE model. Calculations have shown that after a certain period of time after the start of sound emission, the scattered field in the vortex core ceases to be stable. The instability is revealed by a typical periodical in polar angle structure that appears in the pattern of the scattered field. The evolution of this structure is accompanied by an exponential increase of disturbance parameters. The characteristics of this instability, as the growth rate and the azimuthal phase frequency, were found to well match those of the unstable normal modes given by the linear-stability analysis.

¹S. Douady, Y. Couder, and M. E. Brachet, "Direct observation of the intermittency of intense vorticity filaments in turbulence," *Phys. Rev. Lett.* **67**, 983 (1991).

²J. Jiménez, A. A. Wray, P. G. Saffman, and R. S. Rogallo, "The structure of intense vorticity in homogeneous isotropic turbulence," *J. Fluid Mech.* **255**, 65 (1993).

³O. Cadot, S. Douady, and Y. Couder, "Characterization of low pressure filaments in a three-dimensional turbulent shear flow," *Phys. Fluids* **7**, 630 (1995).

⁴F. Bottausci and P. Petitjeans, "Visualization of stretched vortices," in *Vortex Structure and Dynamics, Lecture Notes in Physics*, edited by A. Maurel and P. Petitjeans (Springer, Berlin, 1999), pp. 124–134.

⁵X. Carton and J. McWilliams, "Barotropic and baroclinic instabilities of axisymmetric vortices in a quasi-geostrophic model," in *Mesoscale/Synoptic Coherent Structures in Geophysical Turbulence*, edited by J. Nihoul and B. Jamart (Elsevier, New York, 1989), pp. 225–244.

⁶L. Hultgren, "Stability of swirling flows," *Phys. Fluids* **31**, 1872 (1988).

⁷L. N. Howard and D. L. Matthews, "On the vortices produced in shock diffraction," *J. Appl. Phys.* **27**, 223 (1956).

⁸S. N. Brown, "The compressible inviscid leading-edge vortex," *J. Fluid*

Mech. **22**, 17 (1965).

⁹D. Bershader, "Compressible vortices," in *Fluid Vortices*, edited by S. I. Green (Kluwer, Dordrecht, The Netherlands, 1995), pp. 291–317.

¹⁰L. N. Howard, "On the stability of compressible swirling flow," *Stud. Appl. Math.* **52**, 39 (1973).

¹¹E. G. Broadbent and D. W. Moore, "Acoustic destabilization of vortices," *Philos. Trans. R. Soc. London, Ser. A* **290**, 353 (1979).

¹²W. M. Chan, K. Shariff, and T. H. Pulliam, "Instabilities of two-dimensional inviscid compressible vortices," *J. Fluid Mech.* **253**, 173 (1993).

¹³P. Orlandi and G. Carnevale, "Evolution of isolated vortices in a rotating fluid of finite depth," *J. Fluid Mech.* **381**, 239 (1999).

¹⁴G. Flierl, "On the instability of geostrophic vortices," *J. Fluid Mech.* **197**, 349 (1988).

¹⁵J.-M. Chomaz, M. Rabaud, C. Basdevant, and Y. Couder, "Experimental and numerical investigation of a forced circular shear layer," *J. Fluid Mech.* **187**, 115 (1988).

¹⁶F. Gallaire and J.-M. Chomaz, "Three-dimensional instability of isolated vortices," *Phys. Fluids* **15**, 2113 (2003).

¹⁷P. Gent and J. McWilliams, "The instability of barotropic circular vortices," *Geophys. Astrophys. Fluid Dyn.* **35**, 209 (1986).

¹⁸S. Chandrasekhar, *Hydrodynamic and Hydromagnetic Stability* (Dover, New York, 1954), pp. 277–284.

¹⁹W. Smith and J. McWilliams, "Instability of an axisymmetric vortex in a stably stratified, rotating environment," *Theor. Comput. Fluid Dyn.* **11**, 305 (1998).

²⁰J. Flor and G. van Heijst, "Stable and unstable monopolar vortices in a stratified fluid," *J. Fluid Mech.* **311**, 257 (1996).

²¹M. A. Abramowitz and I. A. Stegun, *Handbook of Mathematical Functions* (Dover, New York, 1972).

²²S. J. Chapman, *MATLAB Programming for Engineers*, 2nd ed. (Brooks-Cole, Pacific Grove, CA, 2002).

²³T. Colonius, S. K. Lele, and P. Moin, "The scattering of sound waves by a vortex: numerical simulations and analytical solutions," *J. Fluid Mech.* **260**, 271 (1994).

²⁴R. Ford and S. G. Llewellyn Smith, "Scattering of acoustic waves by a vortex," *J. Fluid Mech.* **386**, 305 (1999).

²⁵R. R. Mankbadi, R. Hixon, S.-H. Shin, and L. A. Povinelli, "Use of linearized Euler equations for supersonic jet noise prediction," *AIAA J.* **36**, 140 (1998).

²⁶C. Bailly, C. Bogey, and D. Juvé, "Computation of flow noise using source terms in linearized Euler's equations," *AIAA Pap.* 2000-2047, 2000.

²⁷K. Viswanathan and L. N. Sankar, "Towards the direct calculation of noise: fluid/acoustics coupled simulation," *AIAA J.* **33**, 2271 (1995).

²⁸I. S. Men'shov and Y. Nakamura, "Implementation of the variational Riemann problem solution for calculating propagation of sound waves in non-uniform flow fields," *J. Comput. Phys.* **182**, 118 (2002).

²⁹S. K. Godunov, "A difference scheme for numerical computation of discontinuous solution of hydrodynamic equations," *Mat. Sb.* **47**, 271 (1959).

³⁰I. S. Men'shov and Y. Nakamura, "On implicit Godunov's method with exactly linearized numerical flux," *Comput. Fluids* **29**, 595 (2000).

³¹B. van Leer, "Toward the ultimate conservative difference scheme V. A second order sequel to Godunov's method," *J. Comput. Phys.* **32**, 101 (1979).

³²J. E. Fromm, "A method for reducing dispersion in convective difference schemes," *J. Comput. Phys.* **3**, 176 (1968).

³³J. D. Lambert, *Numerical Methods for Ordinary Differential Systems* (Wiley, New York, 1991), Chap. 5.

³⁴I. S. Men'shov and Y. Nakamura, "A Godunov-type method for computational acoustics," *AIAA Pap.* 2000-2329, 2000.

³⁵M. S. Howe, "Contributions to the theory of aerodynamic sound, with application to excess jet noise and the theory of the flute," *J. Fluid Mech.* **71**, 625 (1975).

³⁶A. L. Fabricant, "Sound scattering by vortex flow," *Sov. Phys. Acoust.* **29**, 2 (1983).